

## RESEARCH ARTICLE

10.1002/2016JA022788

## Key Points:

- Direction comparison of EISCAT and SuperDARN derived electron densities
- Test of multiple methods with SuperDARN data
- SuperDARN and EISCAT disagree by large margins

## Correspondence to:

L. K. Sarno-Smith,  
loisks@umich.edu

## Citation:

Sarno-Smith, L. K., M. J. Kosch, T. K. Yeoman, M. Rietveld, A. Nel, and M. W. Liemohn (2016), Ionospheric electron number densities from CUTLASS dual-frequency velocity measurements using artificial backscatter over EISCAT, *J. Geophys. Res. Space Physics*, 121, 8066–8076, doi:10.1002/2016JA022788.

Received 4 APR 2016

Accepted 26 JUL 2016

Accepted article online 30 JUL 2016

Published online 27 AUG 2016

## Ionospheric electron number densities from CUTLASS dual-frequency velocity measurements using artificial backscatter over EISCAT

Lois K. Sarno-Smith<sup>1,2</sup>, Michael J. Kosch<sup>2,3,4</sup>, Timothy Yeoman<sup>3</sup>, Michael Rietveld<sup>5,6</sup>, Amore' Nel<sup>2,7</sup>, and Michael W. Liemohn<sup>1</sup>

<sup>1</sup>Department of Climate and Space Sciences and Engineering, University of Michigan, Ann Arbor, Michigan, USA, <sup>2</sup>South African National Space Agency, Hermanus, South Africa, <sup>3</sup>Physics Department, University of Lancaster, Lancaster, UK, <sup>4</sup>Physics Department, University of Western Cape, Cape Town, South Africa, <sup>5</sup>EISCAT Scientific Association, Kiruna, Sweden, <sup>6</sup>Department of Physics and Technology, University of Tromsø, Tromsø, Norway, <sup>7</sup>Department of Physics and Electronics, North-West University, Potchefstroom, South Africa

**Abstract** Using quasi-simultaneous line-of-sight velocity measurements at multiple frequencies from the Hankasalmi Cooperative UK Twin Auroral Sounding System (CUTLASS) on the Super Dual Auroral Radar Network (SuperDARN), we calculate electron number densities using a derivation outlined in Gillies et al. (2010, 2012). Backscatter targets were generated using the European Incoherent Scatter (EISCAT) ionospheric modification facility at Tromsø, Norway. We use two methods on two case studies. The first approach is to use the dual-frequency capability on CUTLASS and compare line-of-sight velocities between frequencies with a MHz or greater difference. The other method used the kHz frequency shifts automatically made by the SuperDARN radar during routine operations. Using ray tracing to obtain the approximate altitude of the backscatter, we demonstrate that for both methods, SuperDARN significantly overestimates  $N_e$  compared to those obtained from the EISCAT incoherent scatter radar over the same time period. The discrepancy between the  $N_e$  measurements of both radars may be largely due to SuperDARN sensitivity to backscatter produced by localized density irregularities which obscure the background levels.

### 1. Introduction

The Super Dual Auroral Radar Network (SuperDARN) consists of 35 coherent scatter high-frequency (HF) radars stationed throughout the world [Greenwald et al., 1995; Chisham et al., 2007; Baker et al., 2011]. SuperDARN radars record the Doppler velocity of ionospheric plasma irregularities and can provide large area convection maps of the *F* region [Ponomarenko et al., 2008; Thomas et al., 2013]. However, velocity measurements from SuperDARN are determined with assumption that the index of refraction of the scattering volume is 1.0. In reality, the index of refraction is typically closer to 0.8 [Gillies et al., 2009]. This overestimation of the refractive index leads to a consistent underestimation of the Doppler velocity [Eglitis et al., 1998; Davies et al., 1999; Xu et al., 2001].

The estimation of index of refraction can be corrected using ionospheric electron number densities ( $N_e$ ) from models such as the International Reference Ionosphere (IRI) or local ionosonde measurements [Bilitza, 2001]. Since the scattering area of each SuperDARN radar is so large (approximately  $4 \times 10^6$  km<sup>2</sup>), direct comparison can lead to ambiguities due to localized blobs and convection [Norman et al., 2004; de Larquier et al., 2011]. A reliable method to calculate the actual index of refraction from SuperDARN observations will lead to better Doppler velocity measurements from backscatter when plasma irregularities are present.

Gillies et al. [2010, 2012] demonstrated theoretically that the index of refraction can be calculated from dual-frequency observations using SuperDARN. We can subsequently calculate  $N_e$  from the plasma frequency. This method is valid as long as the SuperDARN radar shifts the operating frequency of the radar on a timescale where the ionosphere is stationary and if the difference of ray propagation paths at the two frequencies is small. Gillies et al. [2012] showed statistical results of the derived SuperDARN electron number densities from all the available SuperDARN radars from 1993 to 2012. However, no direct comparison of plasma density between SuperDARN and another independent method was presented. They also compared the observed line-of-sight velocities to those measured by the Defense Meteorological Satellite Program and the European

Incoherent Scatter (EISCAT) radar. The velocities matched extremely well when the index of refraction was accounted for (0.99 best fit line slope) [Gillies *et al.*, 2012].

Links between ionospheric density irregularities, gravity waves, particle precipitation, and satellite drag prompted the need for large coverage and accurate electron number density measurements [Drell *et al.*, 1965; Hooke, 1968; Robinson *et al.*, 1987]. Previous work has calculated electron number densities from SuperDARN measurements using ground scatter [André *et al.*, 1998]. If SuperDARN can provide reliable  $N_e$  measurements, the scientific community will have access to near global  $N_e$  coverage at high latitudes. This would, for example, permit quasi-real-time global studies of Joule heating in the  $E$  region [Kosch and Nielsen, 1995] or  $F$  region [Cierpka *et al.*, 2000].

We expand the Gillies *et al.* [2012] study to directly compare the SuperDARN calculated  $N_e$  to EISCAT incoherent scatter electron number densities. By generating artificial plasma irregularities (striations) with the EISCAT heater [Rietveld *et al.*, 1993] at Tromsø to create an artificial “target” for SuperDARN backscatter, we can then use ray tracing to localize the backscatter and directly compare the SuperDARN radar  $N_e$  with the EISCAT  $N_e$  [Kosch *et al.*, 2004; Wright *et al.*, 2006; Yeoman *et al.*, 2008]. The EISCAT  $N_e$  are derived from incoherent backscatter power accounting for the electron to ion temperature ratio in a fitting procedure using the Grand Unified Incoherent Scatter Design and Analysis Package software [Lehtinen and Huuskonen, 1996]. Our analysis is the first real test on the accuracy of the SuperDARN-based electron density estimates. The analysis tests credibility of the method for global-scale electron density monitoring for the case of multiple-radar utilization. We use the Cooperative UK Twin Located Auroral Sounding System (CUTLASS) Hankasalmi SuperDARN radar (62.32°N, 26.61°E, geographic coordinates) [Lester *et al.*, 2004] for comparison with EISCAT (69.6°N, 19.2°E, geographic coordinates) [Rishbeth and Van Eyken, 1993]. CUTLASS offers the unique advantage of simultaneous transmission and reception of two independent signals. This STEREO capability is powerful since it allows the SuperDARN radar to essentially act as two independent radars. Thus, we can calculate electron densities using simultaneous measurements with 1 MHz or more frequency separation (e.g., 15 and 16 MHz). Different frequency rays will propagate to different altitudes along their paths in the  $F$  region. However, it has been shown that pump-induced artificial striations extend tens of kilometer in altitude [Senior *et al.*, 2004]. So we can reasonably expect backscatter from similar ranges at different frequencies to come from about the same irregularity regions.

The results of our study demonstrate that  $N_e$  calculated from Hankasalmi radar measurements are sensitive to the frequencies used to derive the  $N_e$  and overestimate  $N_e$  compared to EISCAT values. We use two controlled heater experiments, one at daytime and one in the afternoon/evening, to provide artificial backscatter targets and narrow spectral widths in the Hankasalmi line-of-sight velocities. We also show that the method using smaller-frequency shifts on the kHz scale also overestimates  $N_e$  compared to EISCAT.

## 2. Methodology

The index of refraction,  $n_s$ , can be calculated using the plasma frequency  $f_p$  and the radar wave frequency  $f$

$$n_s = \sqrt{1 - f_p^2/f^2} \quad (1)$$

and Gillies *et al.* [2011] showed that  $f_p$  could be calculated using two radar frequency observations of line-of-sight velocity,  $v$

$$f_p^2 = \frac{f_1^2 (1 - v_1^2/v_2^2)}{1 - v_1^2 f_1^2 / v_2^2 f_2^2} \quad (2)$$

Only observations where  $v_1/v_2 < 1$  are physically meaningful for calculating index of refraction in this study. From this, we can calculate  $N_e$  ( $\text{m}^{-3}$ ) from the  $f_p$  (Hz) as

$$N_e = \frac{m_e \epsilon_0}{q^2} (2\pi f_p)^2 \quad (3)$$

where  $m_e$  is the mass of an electron,  $\epsilon_0$  is the permittivity of free space, and  $q$  is the charge of an electron. SuperDARN monofrequency radars, by stepping the frequency every few seconds, can be used to calculate  $N_e$  from  $f_1$  and  $f_2$ . With the dual-frequency STEREO capability, available on Hankasalmi, we operate the radar at two major frequency bands (e.g., 15 and 16 MHz) with incremental steps (kHz) in each band every few seconds.

We use data from two experiments. The first experiment was conducted on 12 March 2015 10:00 to 12:01 UT, or 11:00 to 13:01 LT in Tromsø. During this daytime interval,  $K_p$  was at 2<sup>+</sup>. The CUTLASS Hankasalmi radar (62.3°N, 26.6°E) was operated at 15 and 16 MHz sequentially between 10:00 and 11:21 UT. From 11:22 UT to 12:01 UT, the frequency was shifted between three major frequency bands at 16 MHz, 17 MHz, and 18 MHz. For the first case study, the 15 MHz band contained frequencies between 15.0 and 15.1 MHz, the 16 MHz band contained frequencies from 16.2 to 16.7 MHz, the 17 MHz band contained frequencies from 17.9 MHz to 18.1 MHz, and the 18 MHz band contained frequencies from 18.8 to 18.9 MHz. The radar operated on beam 5 with range gates beginning at 480 km and spaced 15 km apart with 1 s integration on each frequency sequentially, i.e., the cycle was either 2 s or 3 s long.

The EISCAT heater operated with its beam field aligned to the local magnetic field (at a height of 240 km) at 6.2 MHz between 10:00 and 11:21 UT and then changed to 6.96 MHz between 11:21 and 12:01 UT. The radiation from the heater was in ordinary polarization mode. Ionospheric pumping was slightly under dense, where the radiation frequency is greater than the peak plasma frequency, throughout the interval. However, many past experiments have shown this can still produce striations [Leyser *et al.*, 1990; Gurevich *et al.*, 1995]. The effective radiated power (ERP) was 53 MW between 10:00 and 11:21 UT and 32 MW between 11:21 and 12:01 UT.

The second experiment was conducted on 3 March 2016 from 14:00 to 18:00 UT, or 15:00 to 19:00 LT in Tromsø, with  $K_p < 2$  throughout the experiment. Part of the experiment occurred after sunset (approximately 17:00 UT). The CUTLASS Hankasalmi STEREO radar was operated alternating between 13 and 15 MHz on Channel A throughout the entire interval and with, additionally, 16 MHz between 14:00 and 17:00 UT on Channel B. For the second case study, the 13 MHz band contained frequencies between 13.2 and 13.3 MHz, the 15 MHz band contained frequencies between 15.0 and 15.1 MHz, and the 16 MHz band contained frequencies between 16.2 and 16.7 MHz. The radar operated on beam 5 with range gates beginning at 480 km and spaced 15 km apart on Channel A and the range gates beginning at 180 km and incrementing 45 km on Channel B. Channel A operating frequency was varied between 13 and 15 MHz, using 3 s integration with a 6 s cycle time. Channel B measured only at 16 MHz using 3 s integration and also a 3 s cycle time.

The EISCAT ionospheric modification facility operated with the beam pointing field aligned and between 4.04 MHz and 5.423 MHz with 5.423 MHz between 14:00 and 16:30 UT with an ERP of 180 MW, 4.9128 MHz between 16:30 and 16:38 UT with an ERP of 154 MW, 4.544 MHz from 16:38 to 17:38 UT with an ERP of 131 MW, and 4.04 MHz from 17:45 to 18:00 UT with an ERP of 110 MW. Ionospheric heating was mostly overdense, where the radiation frequency was lower than the peak ionospheric plasma frequency, during this experiment with the reflection altitude at approximately 220 km. For both experiments, the EISCAT UHF radar observed field aligned using the 32 × 20 alternating “beata” code with 10 μs sampling. This gives 3 km range resolution, 5 s time integration, and covers between 49 and 694 km in range. The EISCAT  $N_e$  during both experiments were calibrated with local ionosonde measurements.

Figure 1a shows the Hankasalmi radar line-of-sight velocities used in our  $N_e$  calculation between range gates 25 and 38 for the 12 March 2015 experiment. Figure 1 assimilates velocity measurements from 15 to 18 MHz frequencies. Figure 1b shows the spectral widths over the same period. For most of the experiment the velocities are negative and the spectral widths are small (<50 m/s) which is characteristic of backscatter from artificially generated striations.

Figure 2 further demonstrates that the velocity distribution for each frequency is largely contained between 0 and –50 m/s. Figure 2a shows the velocities for 15 MHz, Figure 2b shows 16 MHz velocities, Figure 2c is 17 MHz velocities, and Figure 2d is 18 MHz velocities. The bin widths in the bar plots are 50 m/s. In particular, for the 17 MHz frequency, the velocity distribution is strongly peaked at approximately –50 m/s. The small velocity distribution is consistent with the narrow spectral width and is a feature of backscatter from artificially generated striations.

A ray trace to determine the altitude CUTLASS observes over EISCAT is imperative for our comparison. For the most accurate ray trace, a reliable angle of arrival measurement is necessary. However, the angle of arrival information for Hankasalmi was unavailable during both of our experiments. Figure 3a shows the ray trace between 5 and 40° elevation angles for the 16 MHz frequency channel on beam 5 for 12 March 2015. The silver lines indicate every fourth range gate starting at 480 km (range gate 0). The black star represents the approximate EISCAT radar location. The horizontal black lines represent a ray for every 2° of elevation angle.

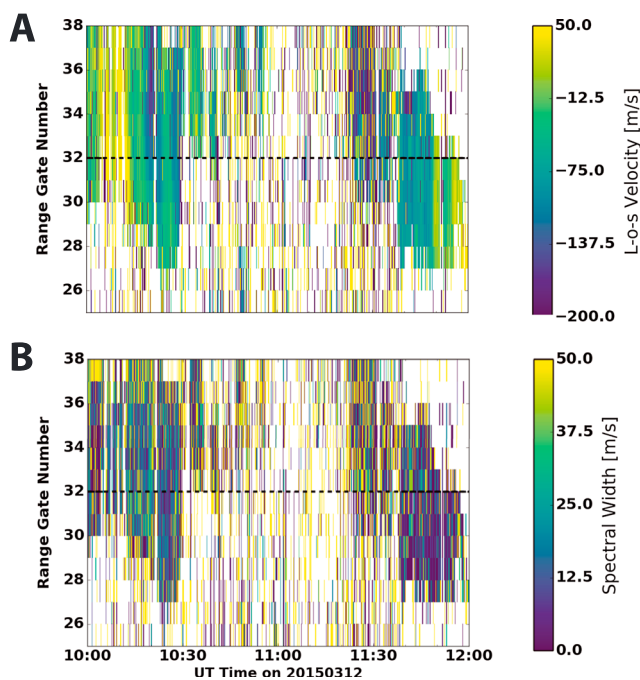


**Figure 1.** (a) The line-of-sight velocities from the Hankasalmi radar at frequencies of 15 MHz–18 MHz on 12 March 2015 from 10:00 UT to 12:00 UT at range gates of 25 to 38. The range gates start at 480 km and have 15 km spacing from there. EISCAT is located at approximately range gate 32, where we have placed a black dotted line. (b) The spectral widths over the same frequencies and same time period.

Based on where the last raypaths that refract back to Earth are over Tromsø, we estimate that Hankasalmi observes between 200 and 260 km, which is consistent with the  $h_m F_2$  peak from the ionosonde measurements on this day at 240 km. For the following figures, we estimate that Hankasalmi observes backscatter from 240 km on this day. When the same elevation angles are compared, higher frequencies probe higher levels of the ionosphere, with a 1 MHz frequency difference producing height differences from 5 km to 50 km. Similar results are obtained for 3 March 2016 (not shown). Here the heater pump frequency corresponded

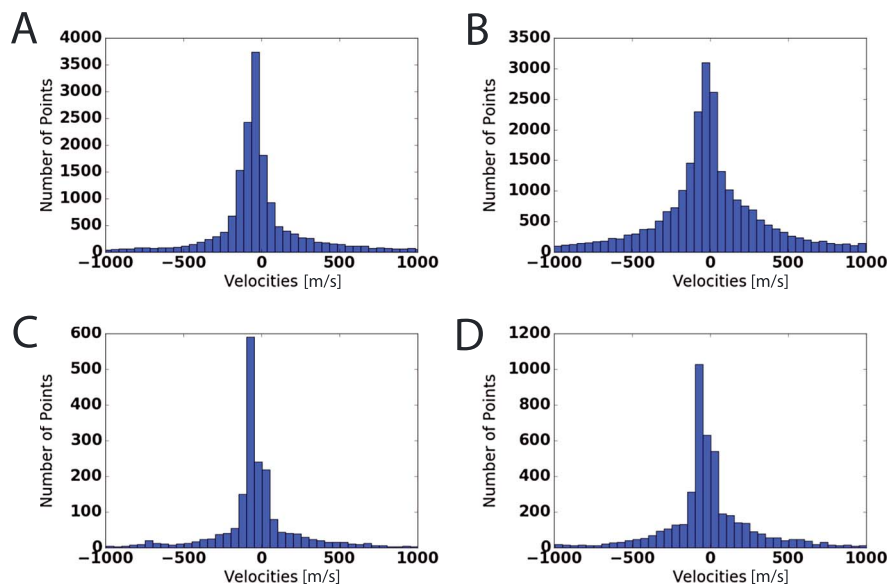


**Figure 2.** Velocity distributions of each of the major frequency bands from the Hankasalmi radar. (a) 15 MHz, (b) 16 MHz, (c) 17 MHz, and (d) 18 MHz for the campaign on 12 March 2015 from 10:00 to 12:00 UT.

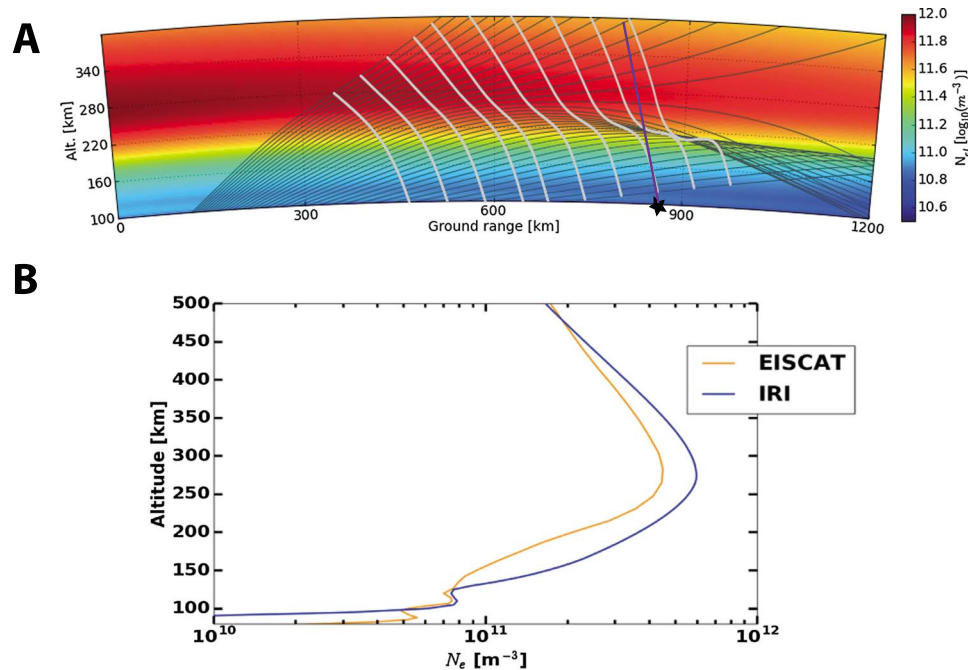


**Figure 3.** (a) The SuperDARN ray tracing model output for our experiment at 16 MHz for beam 5 on 12 March 2015. The radar-beam elevation angle ranges between 5 and 40°, with 2° increments represented by the black lines. The silver lines are every fourth range gate (approximately 60 km) starting at 480 km (range gate 0). The background is  $N_e$  from the IRI model. The black star represents the approximate distance to the EISCAT Tromsø site. The purple line represents the magnetic field line at Tromsø, indicating the look direction of the EISCAT heater. (b) The IRI (blue) and EISCAT (orange)  $N_e$  profiles averaged between 10:00 and 12:00 UT on 12 March 2015.

to the ionospheric plasma frequency at an altitude of approximately 220 km. In Figure 3b, we show the IRI and EISCAT  $N_e$  profiles averaged between 10:00 and 12:00 UT on 12 March 2015 to demonstrate that IRI and EISCAT provide similar  $N_e$  values below 300 km. Since the model values from IRI are close to EISCAT, we can trust the ray trace in Figure 3a which relies on IRI to calculate the index of refraction.

### 3. Results

We test two methods to determine if  $N_e$  can be reliably calculated from SuperDARN radar data. We make use of the unique STEREO feature of the CUTLASS radar at Hankasalmi, when it is available, which was in our experiment on 3 March 2016. At each measurement, we first average the range gates of backscatter where Hankasalmi observes irregularities produced by the EISCAT heater, here defined as range gates 30–35. Then we resample the data to a 2 min cadence in each frequency band. Simultaneous comparison and unaveraged measurements from several range gates result in noisy data, which is why we spatially and temporally smooth the data before calculating the velocity ratio between the two frequencies. If  $v_1 > v_2$ , the  $N_e$  values are unphysical because the derivation of equation (2) from equation (1) assumes that, because the refractive index is dependent on radar frequency, the velocity measured at the lower frequency ( $v_1$ ) must be lower than the velocity measured at the higher frequency ( $v_2$ ). Therefore, we remove all data when  $v_1 > v_2$ . There are four bands we compare from the first case study on 12 March 2015: 15–16 MHz, 16–17 MHz, 17–18 MHz, and 16–18 MHz and three bands from the second case study on 3 March 2016 at 13–15 MHz, 13–16 MHz, and 15–16 MHz.

Table 1 shows the number of points used in the study before resampling the velocities and the number of velocity points in the 2 min resample. For the case study on 12 March 2015, most of the velocity data are measured at 15 MHz (1024 points) or 16 MHz (1365 points) which are then downsampled to 23 points of conjunction between the 15 and 16 MHz frequencies. For the case study on 3 March 2016, there are many points spread between 13 MHz (1089 points), 15 MHz (1562 points), and 16 MHz (1710) while Hankasalmi operated in dual-frequency mode. This led to 39 two-minute interval conjunctions between 13 and 15 MHz,

**Table 1.** The Number of Raw Data Points at Each Frequency and Down-Sampled Data Points for Each Frequency Pair for Both Case Studies

<i>Before Resample</i>		
Frequency (MHz)	2015–03–12	2016–03–03
13	0	1089
15	1024	1562
16	1365	1710
17	185	0
18	168	0
<i>Number of Points After Resample</i>		
13–15	0	39
13–16	0	22
15–16	23	32
16–17	7	0
16–18	14	0
17–18	6	0

22 conjunction points between 13 and 16 MHz, and 32 conjunction points between 15 and 16 MHz. The number of downsampled points in our study is much lower than the  $10^6$  points used in Gillies *et al.* [2010].

The second method is to use the small-frequency shifts of kHz that SuperDARN automatically makes as it scans within a selected frequency range. For instance, in the 15 MHz band we observe an approximate 1 kHz change every 2 s. The radar does this to select the quietest frequency of observation, giving the highest signal-to-noise ratio. Our second method uses this frequency shift by averaging the measurements in range gates 30–35 at a given time and then calculating  $N_e$  from the average line-of-sight velocity measurement and slightly shifted frequency 2 s later. We also remove times when  $v_1 > v_2$ . This method requires assuming ionospheric stability over a 2 s interval but with far smaller-frequency shifts. We then resample these data to a 2 min cadence to reduce the noise of the measurements. The potential advantage of this method is that the dual-frequency STEREO mode of CUTLASS is not necessary and this method could be implemented on all SuperDARN radars.

Figure 4 illustrates the differences in the two approaches for calculating  $N_e$  for both case studies. Figure 4a shows the Hankasalmi data from 12 March 2015. The colored triangles represent the  $N_e$  from wide-frequency spacing, where red is 15–16 MHz, green is 16–17 MHz, yellow is 16–18 MHz, and blue is 17–18 MHz. The monochrome hexagons represent the  $N_e$  calculated from small-frequency shifts (kHz), with black as the 15 MHz measurements, dark grey is the 16 MHz measurements, light grey is the 17 MHz  $N_e$ , and white is the 18 MHz  $N_e$ . Figure 4b shows the Hankasalmi data from 3 March 2016, where the red triangles represent 13–15 MHz, green is 13–16 MHz, and yellow is 15–16 MHz. The grey scale hexagons represent the small-frequency shift calculated  $N_e$ , with black as the 13 MHz measurements, dark grey is the 15 MHz measurements, and light grey is the 16 MHz  $N_e$ .

The most notable feature of this figure is the near constant values the small-frequency shift calculated  $N_e$  exhibits. For example, in Figure 4a, at 15 MHz, the calculated  $N_e$  value barely fluctuates from  $2.7 \times 10^{12} \text{ m}^{-3}$  while the  $N_e$  from 16 MHz hovers at  $3.3 \times 10^{12} \text{ m}^{-3}$ . The  $N_e$  calculated from wide-frequency spacing, on the other hand, shows some variability and changes in time in a more reasonable manner. The lack of variation in the  $N_e$  from small-frequency shifts shows that this method is strongly influenced by the value of  $f_1$  in equation (2), which is the measuring frequency of the line-of-sight velocities. Larger values of  $f_1$  correspond to larger  $N_e$ , with 17 and 18 MHz frequency data being the highest and producing similar values. This is consistent in Figure 4b with 16 MHz producing the largest  $N_e$ . The small-frequency shift method of estimating  $N_e$  produces unrealistically static  $N_e$  values subject to the radar frequency, which is not consistent with expectation.

Figure 5 shows  $N_e$  calculated from the wide-frequency spacing from Hankasalmi compared to EISCAT and IRI  $N_e$  values. The  $N_e$  from Hankasalmi is approximately an order of magnitude larger than the EISCAT and IRI  $N_e$ . The IRI  $N_e$  values are calculated on an hourly timescale during the experiments from the Community Coordinated Modeling Center (CCMC). In Figure 5a, the colored triangles represent the  $N_e$  from Hankasalmi,

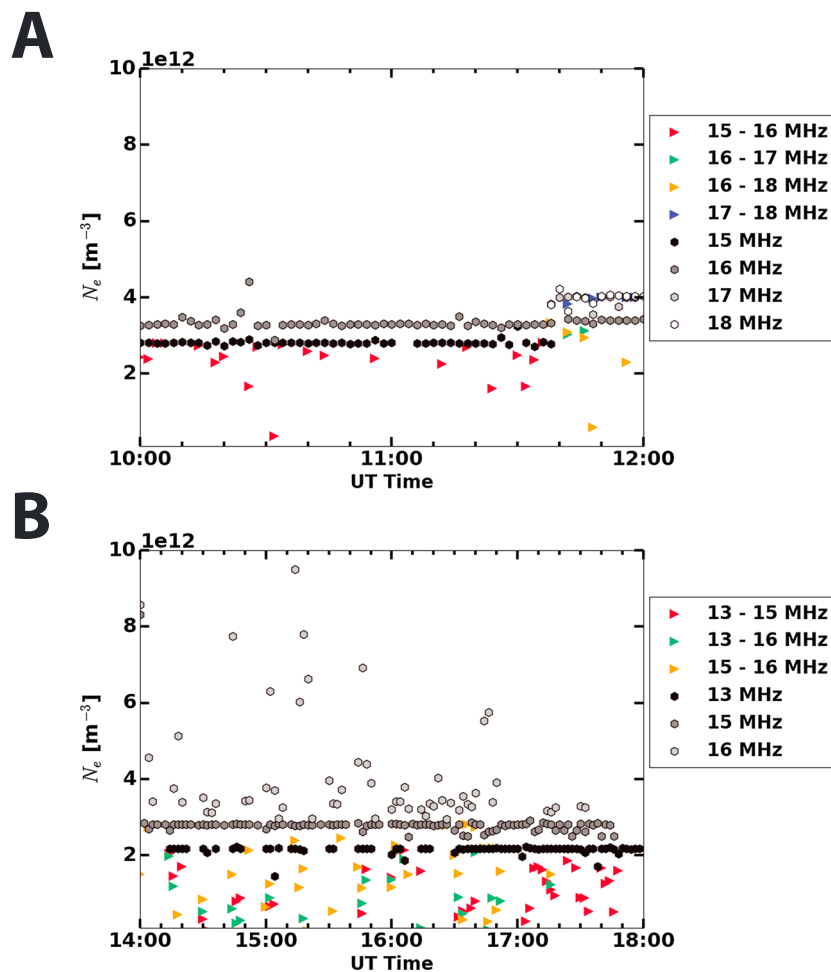


**Figure 4.** The colored triangles represent the Hankasalmi radar STEREO mode data resampled on a 2 min cadence for (a) 12 March 2015 between 10:00 and 12:00 UT. Red is the calculated  $N_e$  from the 15 and 16 MHz frequency measurements, green is the 16 and 17 MHz frequency measurements, yellow is the 16 and 18 MHz frequency measurements, and blue is the 16 and 18 MHz measurements. The monochrome hexagons represent the small-frequency shift (a few kHz) method of calculating  $N_e$  using Hankasalmi data observations over the same time period. The small frequency shifted  $N_e$  are also resampled on a 2 min cadence. Black represents 15 MHz, dark grey is 16 MHz, light grey is 17 MHz, and white is 18 MHz. (b) Similar with  $N_e$  from 3 March 2016 14:00 to 18:00 UT with red as STEREO mode between 13 and 15 MHz, green between 13 and 16 MHz, and gold between 15 and 16 MHz. The monochrome hexagons represent small-frequency shift  $N_e$  calculations, with black as 13 MHz, dark grey as 15 MHz, and light grey as 16 MHz. For both methods in Figures 4a and 4b, the mean line-of-sight velocity over range gates 30–35 at each measurement is used in the calculation.

where red is the 15–16 MHz, green is the 16–17 MHz, yellow is the 16–18 MHz, and blue is the 17–18 MHz observations on 12 March 2015. In Figure 5b, the colored triangles represent the  $N_e$  from Hankasalmi, where red is the 13–15 MHz, green is the 13–16 MHz, and yellow is the 15–16 MHz observations on 3 March 2016. In Figure 5a, the grey diamonds are the 2 min resampled  $N_e$  from EISCAT at 240 km and the dotted blue line is the IRI data over this time range at 240 km. For Figure 5b, EISCAT and IRI  $N_e$  are taken from 220 km.

The Hankasalmi derived  $N_e$  does not capture the  $1 \times 10^{11} \text{ m}^{-3}$  increase that EISCAT measures starting at 10:50 UT in Figure 5a. Instead, the Hankasalmi derived  $N_e$  remains somewhat constant between 10:00 and 11:30 UT and then jumps up by  $1 \times 10^{12} \text{ m}^{-3}$  when different frequencies are employed. Like the small-frequency shift results, this suggests that the  $N_e$  derived from the dual-frequency mode is sensitive to the value of  $f_1$  used in equation (2) and this can affect the results significantly. The IRI and EISCAT  $N_e$  agree very well throughout the time period, with IRI slightly higher than EISCAT.

In Figure 5b, the Hankasalmi derived  $N_e$  completely fails to capture the ionospheric  $N_e$  decrease in the EISCAT data at 16:00 UT. The results from the 3 March 2016 case study are also more variable than the 12 March 2015 case study in Figure 5a, ranging from very close to EISCAT  $N_e$  values to being off by a factor of 20. Once again,

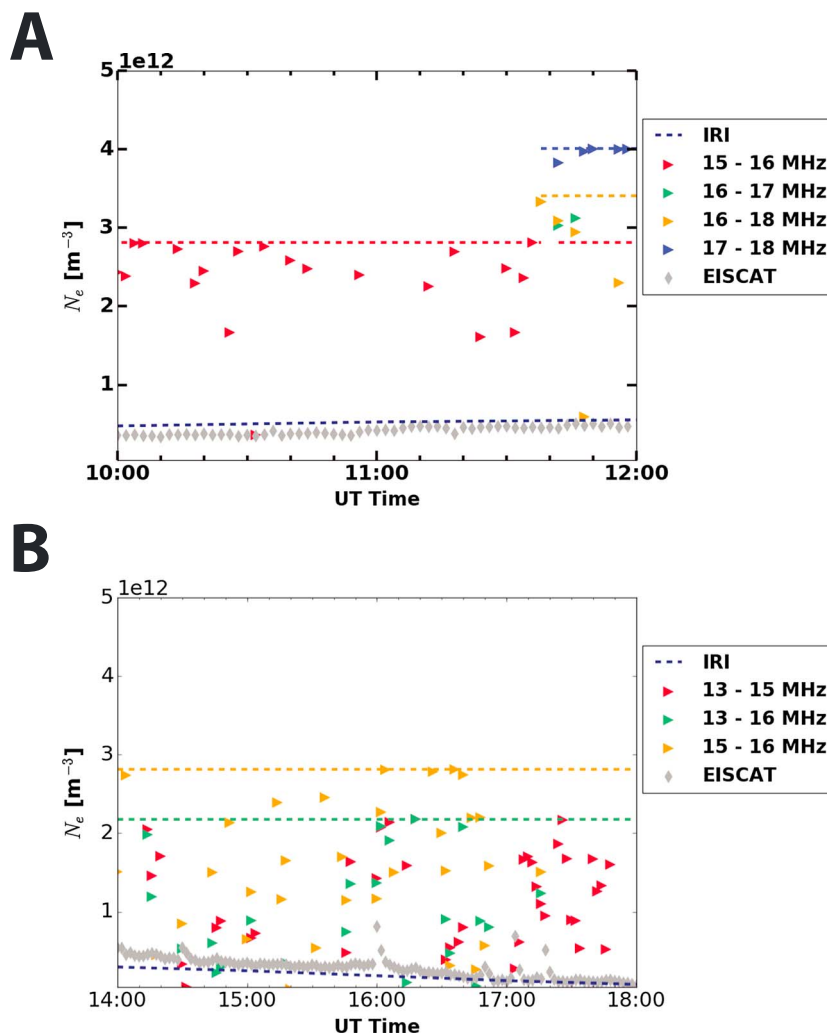


**Figure 5.** The colored triangles are the calculated  $N_e$  from the Hankasalmi STEREO observations for (a) 12 March 2015 from 10:00 to 12:00 UT and (b) 3 March 2016 from 14:00 to 18:00 UT. The shaded diamonds are the EISCAT  $N_e$  at 240 km for Figure 5a and 220 km for Figure 5b. The navy blue dotted line is IRI  $N_e$  at 240 km for Figure 5a and 220 km for Figure 5b. The dashed lines are the maximum electron number density possible in regard to plasma frequency. The color of the triangles and dashed lines indicate what frequency pairs were used to calculate  $N_e$ . In Figure 5a the green line is under the yellow one and in Figure 5b the red line is under the green one.

the IRI and EISCAT  $N_e$  values are very close, with IRI slightly lower than EISCAT in Figure 5b. Overall, the data shown in Figure 5 demonstrate that deriving  $N_e$  from dual-frequency measurements is not a reliable method for calculating background  $N_e$  from SuperDARN measurements.

We also use linear regression to quantify the correlation coefficient ( $r$ ) between the 2 min resampled  $N_e$  from EISCAT and Hankasalmi despite the order of magnitude difference between the data sets. For the first experiment, the  $r$  between 15 and 16 MHz was 0.09, for 16–17 MHz was  $-0.13$ , for 16–18 MHz was 0.03, and for 17–18 MHz was 0.17. For the second experiment, the  $r$  between 13 and 15 MHz was  $-0.049$ , for 13–16 MHz was  $-0.015$ , and between 15 and 16 MHz was  $-0.017$ . All of the linear regression correlation coefficients calculated between the  $N_e$  from Hankasalmi and EISCAT are extremely low, demonstrating that the  $N_e$  derived from Hankasalmi fails to capture the trends measured by EISCAT. On the other hand, the linear regression  $r$  between EISCAT and IRI is 0.97 for the first experiment and 0.99 for the second experiment.

The Hankasalmi  $N_e$  is approximately an order of magnitude larger than the EISCAT  $N_e$ . Figure 6 shows the  $N_e$  from Hankasalmi divided by the EISCAT  $N_e$  at about 240 km, both resampled to the same 2 min cadence between 10:00 to 12:00 UT on 12 March 2015 and 14:00 to 18:00 on 3 March 2016 at approximately 220 km. The black dotted line represents where the Hankasalmi data would match the EISCAT  $N_e$ . The colored triangles

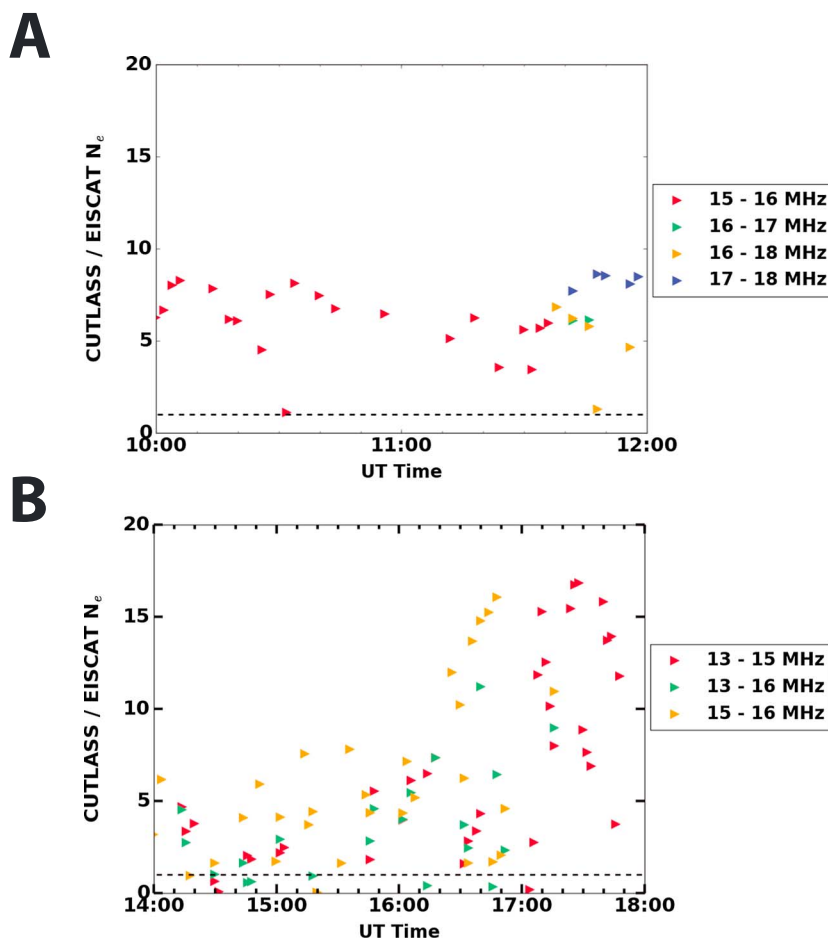


**Figure 6.** The ratio of  $N_e$  calculated from the Hankasalmi and EISCAT radars. The colored triangles are the calculated  $N_e$  from the Hankasalmi STEREO method resampled into 2 min periods for (a) 12 March 2015 from 10:00 to 12:00 UT and (b) 13 March 2016 from 14:00 to 18:00 UT and divided by the EISCAT  $N_e$  at 240 km for Figure 6a and 220 km for Figure 6b at the same times. The black dotted line is where the Hankasalmi  $N_e$  equals the EISCAT  $N_e$ . The color of the triangle indicates what frequency pairs were used to calculate  $N_e$ . In Figure 6a the green line is under the yellow one and in Figure 6b the red line is under the green one.

represent the different frequency bands used to calculate  $N_e$ , as previously described. In Figure 6a, the  $N_e$  derived from the 15–16 MHz observations shows the most variation and difference from the EISCAT  $N_e$  early in the experiment from 10:00 to 10:30 UT. After 10:30 UT, the Hankasalmi  $N_e$  measurements, regardless of frequency, are greater than the EISCAT  $N_e$  by a factor of 6–10. The least variable ratio is the 17–18 MHz band for  $N_e$  measurements, clustered around a factor of 8 difference.

In Figure 6b, all bands (13–15 MHz, 13–16 MHz, and 15–16 MHz) show large variation and are consistently off from the EISCAT  $N_e$ . The offset ratio increases throughout the experiment, reaching a maximum of approximately a factor of 15 by 17:00 UT. This is because the  $N_e$  calculated from Hankasalmi observations do not capture the decrease in the ionosphere as the Sun sets and the ionosphere cools.

With a near order of magnitude overestimate of  $N_e$ , the Hankasalmi measurements do not align well with the EISCAT  $N_e$ . The  $N_e$  derived from Hankasalmi observations also does not capture the gradual increase in  $N_e$  seen by EISCAT after 10:50 UT in the first case study nor the steady decrease of  $N_e$  in the second case study as the Sun sets.

#### 4. Discussion

Theoretically, calculating electron densities from frequency shifts in the SuperDARN line-of-sight Doppler velocity observations should account for the index of refraction and provide reliable electron density calculations. However, our comparison to EISCAT  $N_e$  observations demonstrates that Hankasalmi derived  $N_e$  were

overestimated by approximately a factor 8, which is dependent on the radar frequencies used to calculate  $N_e$ . This demonstrates that the dual-frequency method is not effective for calculating reliable background  $N_e$  from SuperDARN observations.

Gillies *et al.* [2010] proposed that an overestimation of  $N_e$  could be from localized regions of SuperDARN backscatter. For example, dominant scatter could be from a small fraction of the SuperDARN range cell in which conditions for scatter are best. Whereas EISCAT captures the background  $N_e$ , CUTLASS is prone to picking up localized structures which produce stronger irregularities and places with higher electron density [Hosokawa *et al.*, 2009]. Further,  $N_e$  enhancements of up to an order of magnitude due to polar cap patches are likely to occur during the daytime, which is when our experiment on 12 March 2015 took place [Sojka *et al.*, 1990; Pryse *et al.*, 2005]. Polar cap patches have also been shown to extend in the afternoon and evening, which would overlap with the times of our 3 March 2016 case study [Moen *et al.*, 2007; Zhang *et al.*, 2013]. Within a polar cap patch, electron number density can vary by an order of magnitude [Weber *et al.*, 1986]. All of this was mitigated in the experiments presented above by running the EISCAT Heater during these two intervals. This produced plasma irregularities over EISCAT and therefore scattering along the line-of-sight of the Hankasalmi radar, making the Hankasalmi-EISCAT observations ideal for direct comparison.

The field-aligned density striations themselves could also contribute to the SuperDARN  $N_e$  overestimation. Gurevich *et al.* [1999] showed that bunches of field-aligned density striations due to self-focusing of the heater pump beam in the ionosphere could lead to 10%  $N_e$  enhancements. The 10 m scale striations observed by SuperDARN are not large, so the density enhancements would not manifest themselves in the EISCAT  $N_e$  observations but could be selectively picked out by SuperDARN. Several studies have also shown that these field-aligned striations from the EISCAT heating facility produce a strong backscatter response in Hankasalmi measurements [Kelley *et al.*, 1995; Dhillon, 2002; Kosch *et al.*, 2002; Gurevich *et al.*, 2002; Rietveld *et al.*, 2003]. If we could resolve the size of irregularity bunches compared to the scattering volume measured by SuperDARN, it may be possible to reconcile  $N_e$  calculated from SuperDARN observations of line-of-sight velocity measurements at different frequencies with EISCAT  $N_e$ . As stated, though, these striations produce only a 10% density effect, and the Hankasalmi derived  $N_e$  were off by an order of magnitude.

## 5. Conclusions

Our experiments on 12 March 2015 and 3 March 2016 compared calculated  $N_e$ , derived from the CUTLASS Hankasalmi radar line-of-sight velocity measurements, to the Tromsø EISCAT UHF incoherent scatter radar derived  $N_e$ . Our ray tracing estimates showed that Hankasalmi was approximately probing the ionosphere at 240 km over Tromsø on 12 March 2015 and at 220 km on 3 March 2016. We found that the derivation for calculating electron number densities proposed by Gillies *et al.* [2010, 2012] was unsuccessful at determining reasonable background  $N_e$  from pump-induced artificial striations over EISCAT. No plasma density at any altitude could provide agreement. We tested the method using near simultaneous dual-frequency observations (MHz difference) and by also using the automatic frequency shifts (kHz difference) typical of SuperDARN radars when operating on one frequency band. Both methods overestimated  $N_e$  by approximately a factor of 8, and, in particular, the small-frequency shift method resulted in static, frequency-dependent results. Neither method captured EISCAT observed  $N_e$  increases or decreases across the experimental window.

We propose that the overestimation of  $N_e$  by SuperDARN may be due to localized density irregularities dominating the backscatter measured by SuperDARN and resulting in an artificially high  $N_e$  based off of these localized irregularities. However, other factors could contribute to the discrepancy between SuperDARN and EISCAT  $N_e$ , such as the limited number of data points in our case studies.

## References

- André, D., G. J. Sofko, K. Baker, and J. MacDougall (1998), SuperDARN interferometry: Meteor echoes and electron densities from ground scatter, *J. Geophys. Res.*, *103*(A4), 7003–7015.
- Baker, J. B., J. M. Ruohoniemi, A. J. Ribeiro, L. B. Clausen, R. A. Greenwald, N. A. Frisell, and K. A. Sterne (2011), SuperDARN ionospheric space weather, *IEEE Aerosp. Electron. Syst. Mag.*, *26*(10), 30–34.
- Billitz, D. (2001), International Reference Ionosphere 2000, *Radio Sci.*, *36*(2), 261–275.
- Chisham, G., et al. (2007), A decade of the Super Dual Auroral Radar Network (SuperDARN): Scientific achievements, new techniques and future directions, *Surv. Geophys.*, *28*(1), 33–109.
- Cierpka, K., M. J. Kosch, M. Rietveld, K. Schlegel, and T. Hagfors (2000), Ion-neutral coupling in the high-latitude F-layer from incoherent scatter and Fabry Perot interferometer measurements, *Ann. Geophys.*, *18*(9), 1145–1153.

### Acknowledgments

The Michigan coauthors would like to thank the University of Michigan Rackham Graduate school and the NSF GRFP program. EISCAT is an international association supported by research organizations in China (CRIRP), Finland (CSA), Japan (NIPR and STEL), Norway (NFR), Sweden (VR), and the United Kingdom (NERC). Thanks also to the CCMC website for the use of the IRI model, which is available at <http://ccmc.gsfc.nasa.gov/>. The authors would also like to thank the SuperDARN team, in particular Evan Thomas, Kevin Sterne, Xuelling Shi, Jo Baker, and Muhammad Ahunbay for their invaluable assistance in the ray tracing procedure. We would also, in particular, like to thank the NSF GROW with US-AID program for sponsoring this collaboration in conjunction with the NSF GRFP program and the South African National Space Agency (SANSA).

- Davies, J., M. Lester, S. E. Milan, and T. Yeoman (1999), A comparison of velocity measurements from the CUTLASS Finland radar and the EISCAT UHF system, *Ann. Geophys.*, *17*, 892–902.
- de Larquier, S., J. Ruohoniemi, J. Baker, N. Ravindran Varrier, and M. Lester (2011), First observations of the midlatitude evening anomaly using Super Dual Auroral Radar Network (SuperDARN) radars, *J. Geophys. Res.*, *116*, A10321, doi:10.1029/2011JA016787.
- Dhillon, R. S. (2002), Radar studies of natural and artificial waves and instabilities in the auroral ionosphere, PhD thesis, Univ. of Leicester, U. K.
- Drell, S., H. Foley, and M. Ruderman (1965), Drag and propulsion of large satellites in the ionosphere: An Alfvén propulsion engine in space, *J. Geophys. Res.*, *70*(13), 3131–3145.
- Eglitis, P., T. Robinson, M. Rietveld, D. Wright, and G. Bond (1998), The phase speed of artificial field-aligned irregularities observed by CUTLASS during HF modification of the auroral ionosphere, *J. Geophys. Res.*, *103*(A2), 2253–2259.
- Gillies, R., G. Hussey, G. Sofko, K. McWilliams, R. Fiori, P. Ponomarenko, and J.-P. St-Maurice (2009), Improvement of SuperDARN velocity measurements by estimating the index of refraction in the scattering region using interferometry, *J. Geophys. Res.*, *114*, A07305, doi:10.1029/2008JA013967.
- Gillies, R., G. Hussey, G. Sofko, D. Wright, and J. Davies (2010), A comparison of EISCAT and SuperDARN F-region measurements with consideration of the refractive index in the scattering volume, *J. Geophys. Res.*, *115*, A06319, doi:10.1029/2009JA014694.
- Gillies, R., G. Hussey, G. Sofko, P. Ponomarenko, and K. McWilliams (2011), Improvement of HF coherent radar line-of-sight velocities by estimating the refractive index in the scattering volume using radar frequency shifting, *J. Geophys. Res.*, *116*, A01302, doi:10.1029/2010JA016043.
- Gillies, R., G. Hussey, G. Sofko, and K. McWilliams (2012), A statistical analysis of SuperDARN scattering volume electron densities and velocity corrections using a radar frequency shifting technique, *J. Geophys. Res.*, *117*, A08320, doi:10.1029/2012JA017866.
- Greenwald, R., et al. (1995), Darn/SuperDARN, *Space Sci. Rev.*, *71*(1–4), 761–796.
- Gurevich, A., K. Zybin, and A. Lukyanov (1995), Stationary striations developed in the ionospheric modification, *Phys. Rev. Lett.*, *75*(13), 2622.
- Gurevich, A., H. Carlson, M. Kelley, T. Hagfors, A. Karashtin, and K. Zybin (1999), Nonlinear structuring of the ionosphere modified by powerful radio waves at low latitudes, *Phys. Lett. A*, *251*(5), 311–321.
- Gurevich, A., E. Fremouw, J. Secan, and K. Zybin (2002), Large scale structuring of plasma density perturbations in ionospheric modifications, *Phys. Lett. A*, *301*(3), 307–314.
- Hooke, W. H. (1968), Ionospheric irregularities produced by internal atmospheric gravity waves, *J. Atmos. Terr. Phys.*, *30*(5), 795–823.
- Hosokawa, K., K. Shiokawa, Y. Otsuka, T. Ogawa, J.-P. St-Maurice, G. Sofko, and D. Andre (2009), Relationship between polar cap patches and field-aligned irregularities as observed with an all-sky airglow imager at resolute bay and the PolarDARN radar at Rankin Inlet, *J. Geophys. Res.*, *114*, A03306, doi:10.1029/2008JA013707.
- Kelley, M. C., T. L. Arce, J. Salowey, M. Sulzer, W. T. Armstrong, M. Carter, and L. Duncan (1995), Density depletions at the 10-m scale induced by the Arecibo heater, *J. Geophys. Res.*, *100*(A9), 17,367–17,376, doi:10.1029/95JA00063.
- Kosch, M. J., and E. Nielsen (1995), Coherent radar estimates of average high-latitude ionospheric Joule heating, *J. Geophys. Res.*, *100*(A7), 12,201–12,215.
- Kosch, M. J., M. Rietveld, A. Kavanagh, C. Davis, T. Yeoman, F. Honary, and T. Hagfors (2002), High-latitude pump-induced optical emissions for frequencies close to the third electron gyro-harmonic, *Geophys. Res. Lett.*, *29*(23), 2112, doi:10.1029/2002GL015744.
- Kosch, M. J., M. Rietveld, A. Senior, I. McCrea, A. Kavanagh, B. Isham, and F. Honary (2004), Novel artificial optical annular structures in the high latitude ionosphere over EISCAT, *Geophys. Res. Lett.*, *31*(12), L12805, doi:10.1029/2004GL019713.
- Lehtinen, M. S., and A. Huuskonen (1996), General incoherent scatter analysis and GUISDAP, *J. Atmos. Terr. Phys.*, *58*(1), 435–452.
- Lester, M., et al. (2004), STEREO CUTLASS—A new capability for the SuperDARN HF radars, *Ann. Geophys.*, *22*, 459–473.
- Leyser, T., B. Thidé, H. Derblom, Å. Hedberg, B. Lundborg, P. Stubbe, and H. Kopka (1990), Dependence of stimulated electromagnetic emission on the ionosphere and pump wave, *J. Geophys. Res.*, *95*(A10), 17,233–17,244.
- Moen, J., N. Gulbrandsen, D. Lorentzen, and H. Carlson (2007), On the MLT distribution of F region polar cap patches at night, *Geophys. Res. Lett.*, *34*, L14113, doi:10.1029/2007GL029632.
- Norman, R., et al. (2004), Comparing HF radar backscatter from the southern ocean with ray-tracing results using the IRI model, in *Proceedings of the Workshop on the Applications of Radio Science*, pp. 18–20, National Committee for Radio Science, Hobart, Tasmania.
- Ponomarenko, P., C. Waters, and F. Menk (2008), Effects of mixed scatter on SuperDARN convection maps, *Ann. Geophys.*, *26*, 1517–1523.
- Pryse, S., K. Dewis, R. Balthazor, H. Middleton, and M. Denton (2005), The dayside high-latitude trough under quiet geomagnetic conditions: Radio tomography and the CTIP model, *Ann. Geophys.*, *23*, 1199–1206.
- Rietveld, M., H. Kohl, H. Kopka, and P. Stubbe (1993), Introduction to ionospheric heating at Tromsø. Experimental overview, *J. Atmos. Terr. Phys.*, *55*(4), 577–599.
- Rietveld, M., M. J. Kosch, N. Blagoveshchenskaya, V. Kornienko, T. Leyser, and T. Yeoman (2003), Ionospheric electron heating, optical emissions, and striations induced by powerful HF radio waves at high latitudes: Aspect angle dependence, *J. Geophys. Res.*, *108*, 1141.
- Rishbeth, H., and A. Van Eyken (1993), EISCAT: Early history and the first ten years of operation, *J. Atmos. Terr. Phys.*, *55*(4), 525–542.
- Robinson, R., R. Vondrak, K. Miller, T. Dabbs, and D. Hardy (1987), On calculating ionospheric conductances from the flux and energy of precipitating electrons, *J. Geophys. Res.*, *92*(A3), 2565–2569.
- Senior, A., M. T. Rietveld, N. Borisov, M. Kosch, and T. Yeoman (2004), Multi-frequency HF radar measurements of artificial F-region field-aligned irregularities, *Ann. Geophys.*, *22*(10), 3503–3511.
- Sojka, J. J., R. W. Schunk, and J. Whalen (1990), The longitude dependence of the dayside F region trough: A detailed model-observation comparison, *J. Geophys. Res.*, *95*(A9), 15,275–15,280.
- Thomas, E., J. Baker, J. Ruohoniemi, L. Clausen, A. Coster, J. Foster, and P. Erickson (2013), Direct observations of the role of convection electric field in the formation of a polar tongue of ionization from storm enhanced density, *J. Geophys. Res. Space Physics*, *118*(3), 1180–1189.
- Weber, E., J. Klobuchar, J. Buchau, H. Carlson, R. Livingston, O. Beaujardiere, M. McCready, J. Moore, and G. Bishop (1986), Polar cap F layer patches: Structure and dynamics, *J. Geophys. Res.*, *91*(A11), 12,121–12,129.
- Wright, D., J. Davies, T. K. Yeoman, T. Robinson, and H. Shergill (2006), Saturation and hysteresis effects in ionospheric modification experiments observed by the CUTLASS and EISCAT radars, *Ann. Geophys.*, *24*, 543–553.
- Xu, L., A. Koustov, J. Thayer, and M. McCready (2001), SuperDARN convection and Sondrestrom plasma drift, *Ann. Geophys.*, *19*, 749–759.
- Yeoman, T. K., G. Chisham, L. Baddeley, R. Dhillon, T. Karhunen, T. Robinson, A. Senior, and D. Wright (2008), Mapping ionospheric backscatter measured by the SuperDARN HF radars—Part 2: Assessing SuperDARN virtual height models, *Ann. Geophys.*, *26*(4), 843–852.
- Zhang, Q.-H., et al. (2013), Direct observations of the evolution of polar cap ionization patches, *Science*, *339*(6127), 1597–1600.